Available online at www.sciencedirect.com
ScienceDirect
Trans. Nonferrous Met. Soc. China 28(2018) 2236−2247
Transactions of Nonferrous Metals Society of China
www.tnmsc.cn

Elemental micro-segregation characteristic of fiber laser welded Hastelloy C-276 sheet

Kalinga Simant BAL[1], Jyotsna DUTTA MAJUMDAR[2], Asimava ROY CHOUDHURY[1]

1. Department of Mechanical Engineering, Indian Institute of Technology, Kharagpur, West Bengal 721302, India;
2. Department of Metallurgical & Materials Engineering,
Indian Institute of Technology, Kharagpur, West Bengal 721302, India

Received 11 January 2018; accepted 3 June 2018

Abstract: The elemental micro-segregation characteristic within the weld zone for ytterbium fiber laser welded Hastelloy C-276 sheet was investigated. The analysis of segregation ratio and equilibrium distribution coefficient of elements, determined through EDS data, indicate the reduction in micro-segregation of elements compared with the previous reported literatures for laser welded Hastelloy C-276. High melting efficiency of ytterbium fiber laser, reduction in the amount of linear heat input, and high cooling rate of the mushy zone lead to the reduction in micro-segregation. The melting efficiency of ytterbium fiber laser for welding of Hastelloy C-276 of 64% is higher than that (48%) of conventional welding methods. High melting efficiency leads to the reduction in the linear heat input required for welding. Hence, in the present investigation, the same was found to substantially reduce as compared to the previous reported literature. The cooling rate from liquidus temperature to solidus temperature at the weld centerline was found to be in the order of 10^3 °C/s. Cellular dendritic substructure that constituted for lower micro-segregation was formed at the weld centerline.

Key words: Hastelloy C-276 alloy; laser welding; fiber laser; micro-segregation

1 Introduction

Hastelloy C-276 is a versatile Ni-based superalloy having optimized combination of mechanical strength and corrosion resistance [1]. Constituting elements like Cr, Mo and W provide solid−solution strengthening and corrosion resistance to Hastelloy C-276 matrix, while the presence of metal carbide provides grain boundary strengthening [2]. JUN et al [3] have reported the use of such a Ni-based superalloy in the manufacture of heat exchangers, vessels, and pumps, specifically in chemical and marine industries. Other critical areas of applications of Hastelloy C-276 include aerospace, power industry and power stations, where there is often the requirement of welding [4−6]. Linear heat input, defined as the ratio of incident power to welding speed [7], is an important parameter for joining of materials. In cases where welding is carried out at different sheet thicknesses, linear heat input per unit thickness of sheet is used for comparison. Difficulty of welding Ni-based superalloys including Hastelloy C-276 with conventional high heat input fusion joining technique such as gas tungsten arc welding includes the hot cracking tendency due to formation of secondary intermetallic phases because of micro-segregation in the weld zone [8], and the reduction in weldability due to large grain size [9]. LI et al [10] reported that hot cracks occur in Ni−Mo−Cr superalloy when heated at 1365 °C, which is due to the combined effect of localized melting of primary metal carbides and surrounding Si-rich matrix. They also observed that the formation of hot cracks depends on the segregation degree of elements to the liquid film. SIHOTANG et al [11] have reported a reduction in tensile properties of gas tungsten arc welded Hastelloy X in high heat input condition due to the formation of grain boundary liquation film. High heat input also causes the reduction in corrosion resistance of the welded Hastelloy C-276 sample due to non-uniformity in composition of the weld zone [2]. The advantage of lower heat input welding techniques such as laser beam welding includes the reduction in micro-segregation due to faster cooling rate [2], and the production of defect-free welds [12]. ÇAM et al [12] carried out welding of 3 mm-thick

Corresponding author: Asimava Roy CHOUDHURY; Tel: +91-9434036694; E-mail: archie@mech.iitkgp.ac.in
DOI: 10.1016/S1003-6326(18)64868-X

Inconel 718 and Inconel 625 with 2 kW Nd:YAG laser, and obtained crack-free welds with joint efficiencies of 91% and 95%, respectively. ÇAM and KOÇAK [9,13] have extensively studied the joining of various intermetallic alloys such as Ti_3Al, Ni_3Al, Fe_3Al and Al−Li by different welding techniques ranging from conventional welding techniques (GTA, gas flame) to solid state joining (friction stir welding, diffusion bonding) to high energy density beam processes (laser beam welding, electron beam welding). They have compared the mechanical properties of aforementioned alloys joined by low and high heat input processes. In another study, ÇAM and İPEKOĞLU [14] have reported that arc welding for Al alloys affects mechanical strength due to overaging of heat affected zone (HAZ) grains. Since friction stir welding (FSW) does not necessarily lead to strength loss of the weld zone, and its degree of overaging is less as compared to other welding processes, FSW provides another alternative for joining different grades of Al alloys. THIRUNAVUKARASU et al [15], while carrying out diffusion welding of dissimilar metals, have reported that the formation of brittle intermetallic phases occurs in the weld zone due to diffusion of elements. ADABI and AMADEH [16] have carried out heat treatment of Ni coating on 6061 Al substrate, and reported that the composition of intermetallic phase depends on the dominant diffusing element. XU et al [17] have reported that if the Mo concentration exceeds the solubility limit of TiAl alloy matrix, the formation of Mo-rich intermetallic phase occurs in the interdendritic region. QUAN et al [18] carried out gas tungsten arc welding of 2219 Al alloy under three different welding conditions, and observed that the tensile strength of the weld decreased with the increase of the segregation of Cu. ZOU et al [19] have reported that the cast 7075 Al alloy contains high degree of solute segregation, while the solute segregation of the same alloy after solution heat treatment is eliminated because of the diffusion of solute element into the matrix. DUPONT et al [2] have reported that post weld heat treatment can be effective in eliminating any concentration gradient of elements within the weld zone, and can bring about the homogenization of the welded structure. To study the extent of micro-segregation, ratios of elemental composition between diffusion regions are obtained. MORITA and YOSHIKAWA [20] have used impurity segregation ratios between solid Si and Si−Al solvent to study the achievable diffusion of Si for making high purity solar grade silicon. Similarly, QIN et al [21] have defined segregation coefficient as the ratio of elemental composition in the dendrite core to that in the interdendritic region to study the segregation behavior in Ni-based superalloy. It has been reported that the element with segregation coefficient close to 1 has lower tendency to segregate [2].

LUO et al [22] carried out vacuum brazing of Hastelloy C-276 plates using Ni-based filler metal, and observed the variable segregation of Ni, Cr and Mo on different sections of the brazed joint. Welding of Hastelloy C-276 sheet has been a subject of interest for researchers in an attempt to reduce micro-segregation within the weld zone. MA et al [23] performed pulsed Nd:YAG laser welding of 0.5 mm-thick Hastelloy C-276 foil, and did not observe significant macro- and micro-segregation in the weld zone. WU et al [24] did not observe new phase formation by X-ray diffraction analysis of the weld zone for pulsed Nd:YAG laser beam welded Hastelloy C-276 foil. MANIKANDAN et al [25] observed that micro-segregation was reduced by pulsed current gas tungsten arc welding of Hastelloy C-276 due to higher cooling rate as compared to conventional gas tungsten arc welding. Hence, efforts are being made to further reduce the solidification time of the weld zone from liquidus temperature to solidus temperature in order to reduce the extent of micro-segregation [2]. Diode laser pumped ytterbium optical fiber laser beam provides suitable characteristic features like high beam quality as well as appreciable melting efficiency [26,27]. Higher melting efficiency implies less heat loss and thus lower linear heat input is required for melting unit volume of the material. These features of the fiber laser could be used to study the micro-segregation characteristic as there are no reports on welding of Hastelloy C-276 sheets by ytterbium fiber laser. In the present investigation, close-square autogenous butt welding of Hastelloy C-276 sheets with 2.7 mm in thickness by ytterbium optical fiber laser in continuous wave mode was made. This was followed by analysis of elemental micro-segregation characteristic of the weld zone through different microscopic techniques.

2 Experimental

2.1 Pre-welding procedure

Hastelloy C-276 sheets were received in mill annealed condition [1], i.e. sheets were solution-treated at 1120 °C in furnace under argon gas environment, with a holding time of 10 min, followed by rapid air quenching. Table 1 shows the nominal chemical composition of as-received Hastelloy C-276 sheet

Table 1 Nominal chemical composition of as-received Hastelloy C-276 sheet obtained by XRF (mass fraction, %)

Ni	Cr	Mo	Co	W	Fe
56.63	16.04	15.66	0.70	3.15	7.09

Si	Mn	C	V	P	S	Others
0.04	0.53	0.01	0.11	0.03	0.01	Bal.

obtained by X-ray fluorescence (XRF) spectroscopic analysis. Figure 1(a) shows the scanning electron micrographic image of as-received Hastelloy C-276 sheet metal used in the present investigation. From Fig. 1(a) it may be noted that, the microstructure of the as-received base metal is mainly equi-axed crystal having distinct grain boundary. Similar microstructure of as-received base metal has been reported previously [4,25,28,29]. It could be observed from the magnified image of the grain boundary (Fig. 1(b)) that, the network of discontinuous blocky precipitates constitutes the boundary. DUPONT et al [2] have reported similar microstructure at the grain boundary of annealed Ni-based superalloy, and observed that grain boundary precipitates are mainly carbides of Cr, Mo and W. MOHAMED and MOHAMED [30] have also observed spherical precipitates along the grain boundaries of solution-treated Hastelloy C-22 alloy. Hastelloy C-276 sheet with dimensions of 30 mm × 20 mm × 2.7 mm as shown in Fig. 1(c) was prepared for the welding experiment. Sample was rigidly clamped to the fixture and autogenous butt welding was carried out under argon gas shielding environment at a flowing rate of 5 L/min and 1×10^5 Pa. 2 kW ytterbium optical fiber laser system with a wavelength of 1070 nm, a focal length of 200 mm and a focal spot diameter of 0.45 mm was used for welding in continuous wave mode. The laser facility is capable of delivering maximum output power of 1250 W, with computer numerical control laser-head and optical fiber delivery system. Laser beam was focused on the sample surface at the joint interface and welding was carried out using an incident laser power of 1 kW and a welding speed of 1 m/min.

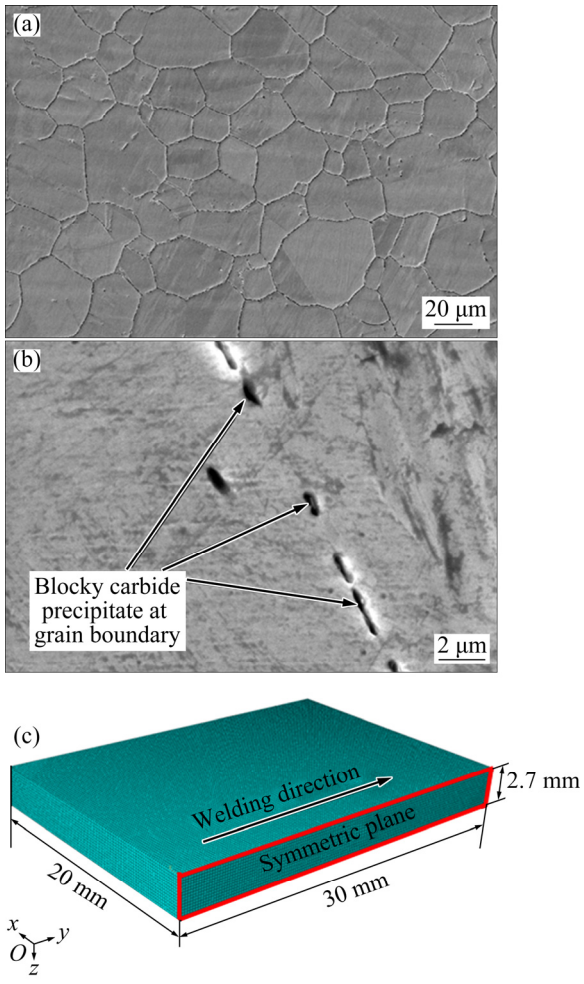

Fig. 1 SEM image of as-received Hastelloy C-276 (a), magnified image of grain boundary (b) and sheet dimension used for welding experiment as well as for finite element method modeling (c) (The border of the symmetric plane is marked in red)

In the present investigation, the cooling rate has been measured by experiment and finite element method (FEM), and the details of which are mentioned below.

(1) Cooling rate measurement by experiment. Temperature cycle of fusion zone during the welding process was recorded by CTLM−2HCF3−C3H infrared pyrometer coupled with a (1064±25) nm notch filter. The calibrated temperature range of the detector was found to vary between 785 and 3260 °C [31]. Infrared pyrometer was focused at the centre of weld track, and the temperature was recorded for every 1 ms (i.e. time response 1 ms) and stored in the computer by CompactConnect 1.8.5.14 software.

(2) Cooling rate measurement by finite element method. A combination of 3D conical volume heat source and cylindrical heat source [32,33] was used for the prediction of the shape of the weld bead as well as cooling rate for the present investigation. The selection of the combined heat source model was based on the experimentally obtained weld bead cross-sectional geometry. For example, LIU and HE [34] have used heat flux with Gaussian distribution to carry out numerical simulation of conical shaped weld pool obtained by electron beam welding of 2219 Al alloy plate. Similarly, according to the shape of the weld bead, ZHANG et al [35] have used rotated parabola body heat source model to study temperature distribution and residual stress for electron beam welded dissimilar alloys. The thermo-physical properties for Hastelloy C-276 were obtained from the data plotted by GUO et al [36]. The finite element model analysis was carried out in ABAQUS CAE 6.10-1 software with dimension of the part same as that used in the experiment and is shown in Fig. 1(c). To save computation time, the symmetry of geometry was considered by selecting symmetric plane along the laser beam scanning direction. A total of 225000 linear hexahedral elements of type DC3D8 and 244016 nodes were considered for meshing the part. A fine and uniform mesh was used throughout the sheet to capture the dynamics of the welding process more

accurately. Convection and radiation modes of heat transfer were considered on the surface exposed to the ambient atmosphere (27 °C) except for the symmetric plane. The temperature cycle was studied at a node located at the weld centerline which fell inside the region at which pyrometer was focused.

2.2 Post-welding procedure

The welded sheet was sectioned, polished and chemically etched in the solution with 15 mL hydrochloric acid + 10 mL nitric acid + 10 mL acetic acid [37]. Microstructural analysis was carried out by scanning electron microscopy (SEM) at an accelerating voltage of 20 kV, a beam current of 100 μA, a probe current of 100 pA and a spot size of 400. Energy-dispersive X-ray spectroscopic (EDS) analysis for elemental composition was carried out at various sites of interest with a probe current of 400 μA. Transmission electron microscopy (TEM) analysis was carried out in Analytical TEM operating at 200 kV after the sample was thinned by ion-milling.

3 Results and discussion

3.1 Summary of observations for present investigation

Tables 2−4 show the comparison of results between the previous reported literature [23] and present investigation on the basis of linear heat input, micro-segregation and equilibrium distribution co-efficient respectively. The details of discussion for the following observations are provided in the next sections onwards.

Table 2 Comparison of results between previous reported literature [23] and present investigation based on linear heat input and linear heat input per unit thickness of sheet

Resource	Linear heat input/(J·mm^{-1})	Linear heat input per unit thickness of sheet/(J·mm^{-1})
MA et al [23]	150*	300*
Present investigation	60	22

*Calculated based on data provided in literature [23]

Table 3 Comparison of results between previous reported literature [23] and present investigation based on EDS data of micro-segregation in weld zone

Resource	Site of interest	Mass fraction/%				
		Ni	Cr	Mo	W	Fe
MA et al [23]	Grain boundary	53.70	16.15	17.88	5.34	5.33
	Grain	59.81	14.73	13.96	4.60	5.80
Present investigation	Interdendritic space	51.55	16.50	20.88	4.88	6.20
	Dendrite body	55.14	16.89	16.79	4.09	7.08

Table 4 Comparison of results between previous reported literature [23] and present investigation based on equilibrium distribution coefficient [2]

Resource	Equilibrium distribution coefficient (k)				
	Ni	Cr	Mo	W	Fe
MA et al [23]	1.01*	0.92	0.90	1.39	1.04
Present investigation	1.00	1.04	0.94	0.84	1.15

*Calculated based on data in literature [23]

3.2 Analysis of linear heat input delivered to weld zone

The value of linear heat input (as well as linear heat input per unit thickness of sheet) for the present investigation was found to be less than that in the other case of study [23]. This might be due to following reasons.

(1) Small laser beam focus diameter of ytterbium optical fiber laser. Spot diameter for Nd:YAG laser is generally 0.60 mm [5,36] as compared to that of 0.45 mm in the present investigation. So, the power density of laser beam used for the present investigation is high, which results in the requirement of lower value of linear heat input. Small beam divergence of ytterbium fiber laser is also another factor for increasing the power density of the laser beam.

(2) High melting efficiency of fiber laser. A comparison between previous studies [4,8,23,25] and present investigation based on melting efficiency of different joining techniques for welding of Hastelloy C-276 could not be made due to unavailability of literatures. The melting efficiency of ytterbium optical fiber for the present investigation was found by conducting experiment at different combinations of laser powers (i.e. 1000 and 1200 W) and welding speed (i.e. 800, 900, 1000, 1100, 1200, 1300 and 1500 mm/min). A linear relation between two dimensionless parameters (i.e. laser speed and laser power parameters [26,27]) was found, as shown in Fig. 2. Constituent factors of both the dimensionless parameters and their respective values are shown in Table 5. It should be noted that values for physical and thermal properties of the Hastelloy C-276 presented in Table 5 were considered at room temperature [1].

Figure 2 shows that the melting efficiency of ytterbium optical fiber laser for the present investigation is found to be 64%, which is higher than the threshold value (i.e. 48%) of melting efficiency for a moving heat source [38,39]. Approximately 64% of the energy is utilized in melting of unit volume of Hastelloy C-276 sheet. A wavelength of 1070 nm allows for efficient absorption of low divergent laser beam on the surface of the Hastelloy C-276 sheet. This reduces the required

amount of linear heat input as well as makes ytterbium fiber laser-welding a cost efficient alternative.

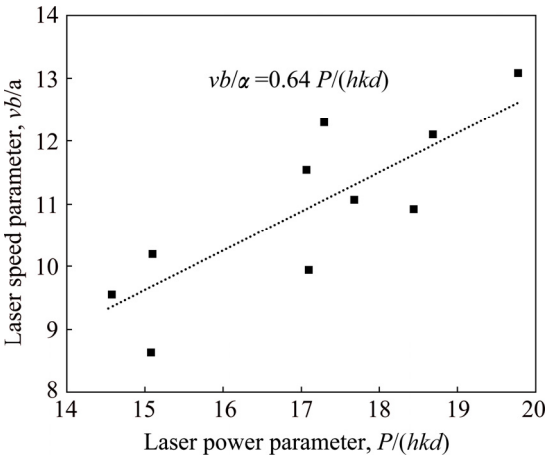

Fig. 2 Melting efficiency of ytterbium fiber laser for welding of 2.7 mm-thick Hastelloy C-276 sheet

Table 5 Constituent factors and their respective values

Constituent factor	Value
Welding speed, v/(m·s^{-1})	0.013, 0.015, 0.016, 0.018, 0.020, 0.021, 0.025
Weld bead width, b/m	Measured after experiment
Diffusivity, α/(m^2·s^{-1})	2.63 ×10^{-6}
Incident laser power, P/kW	1, 1.2
Depth of penetration, h/m	Measured after experiment
Thermal conductivity, k/(W·m^{-1}·K^{-1})	10
Temperature constant [26], d/K	2282
Specific heat capacity, c_p/(J·kg^{-1}·K^{-1})	427
Density, ρ/(kg·m^{-3})	8890
Latent heat of fusion, H/(J·kg^{-1})	4×10^5

3.3 Analysis of elemental micro-segregation within weld zone

Figure 3(a) shows a cellular dendritic substructure with secondary arms formed at the centerline of the weld zone. These substructures are formed when the thermal gradient is high, and solute enrichment ahead of the solid/liquid interface is lower as compared to columnar dendrites and equiaxed structures [40,41]. Figures 3(a) and (b) show the interdendritic space (indicated by Spectrum 3) and dendrite body (indicated by Spectrum 4) respectively, at which the EDS analysis was undertaken. Figure 3(c) shows the intercellular space and cellular substructures formed in the fusion zone. The cellular substructures are formed at the fusion line where the thermal gradient is relatively high as compared with the thermal gradient at the weld centerline. Figure 3(e) shows the presence of cellular substructures at the fusion line, i.e. at the interface of the weld zone and heat affected zone (HAZ). Figures 3(c) and (d) show the intercellular space (indicated by Spectrum 1) and cellular body (indicated by Spectrum 2) respectively, at which the EDS analysis was undertaken. The transition of cellular substructures to cellular dendritic substructure takes place while the grain grows towards the weld centerline. It could be observed from the Fig. 3(f) that cellular dendritic substructures have extended from the fusion line to the weld centerline. Figures 3(g) and (h) show the formation of cellular dendritic substructure at the weld crown and the weld root, respectively. Hence, it could be observed that cellular dendritic substructures are formed mostly throughout the fusion zone. LAMPMAN [41] have also reported the formation of cellular and cellular dendritic substructures in the fusion zone for most of the welded sample.

Table 6 shows the EDS data for fusion zone at interdendritic space and dendrite body carried out at seven different sites of interest (i.e. No. 1−7), and at intercellular space and cellular body carried out at three different sites of interest (i.e. No. 8−10) for sample welded at a laser power of 1 kW and a welding speed of 1 m/min. EDS analysis was carried out at different sites to check the repeatability of the segregation trend at each location.

It was observed that compositions of Cr, Fe, and W at interdendritic space and dendrite body as well as intercellular space and cellular body within fusion zone at ten different site of interest (i.e. No. 1−10) were not found to vary significantly, except for Ni and Mo. The EDS data were validated by the X-ray maps carried out at 20000X for cellular dendritic solidification and shown by Fig. 4. The distribution of elements within the mapped area (that consists of part dendrite body and part interdendritic spacing) showed the degree of segregation for Ni and Mo. Hence during solidification, the concentration of Mo was higher in the liquid phase than that in the solid dendrite body, while the opposite was true for Ni.

ZHANG and LI [42] have used the segregation ratio C_1 (or C_2)/C_3 (or C_4) to quantitatively determine the segregation tendency of an element between interdendritic space and dendrite body as well as between intercellular space and cellular body. C_1 represents the composition (mass fraction, %) of the element in the interdendritic space, and C_2 represents the composition (mass fraction, %) of the element in the intercellular space. Similarly, C_3 represents the composition (mass fraction, %) of the element in the dendrite body, and C_4 represents the composition (mass fraction, %) the element in the cellular body. The segregation ratio, presented in Table 7, has been calculated with the available EDS data (i.e. shown in Table 6).

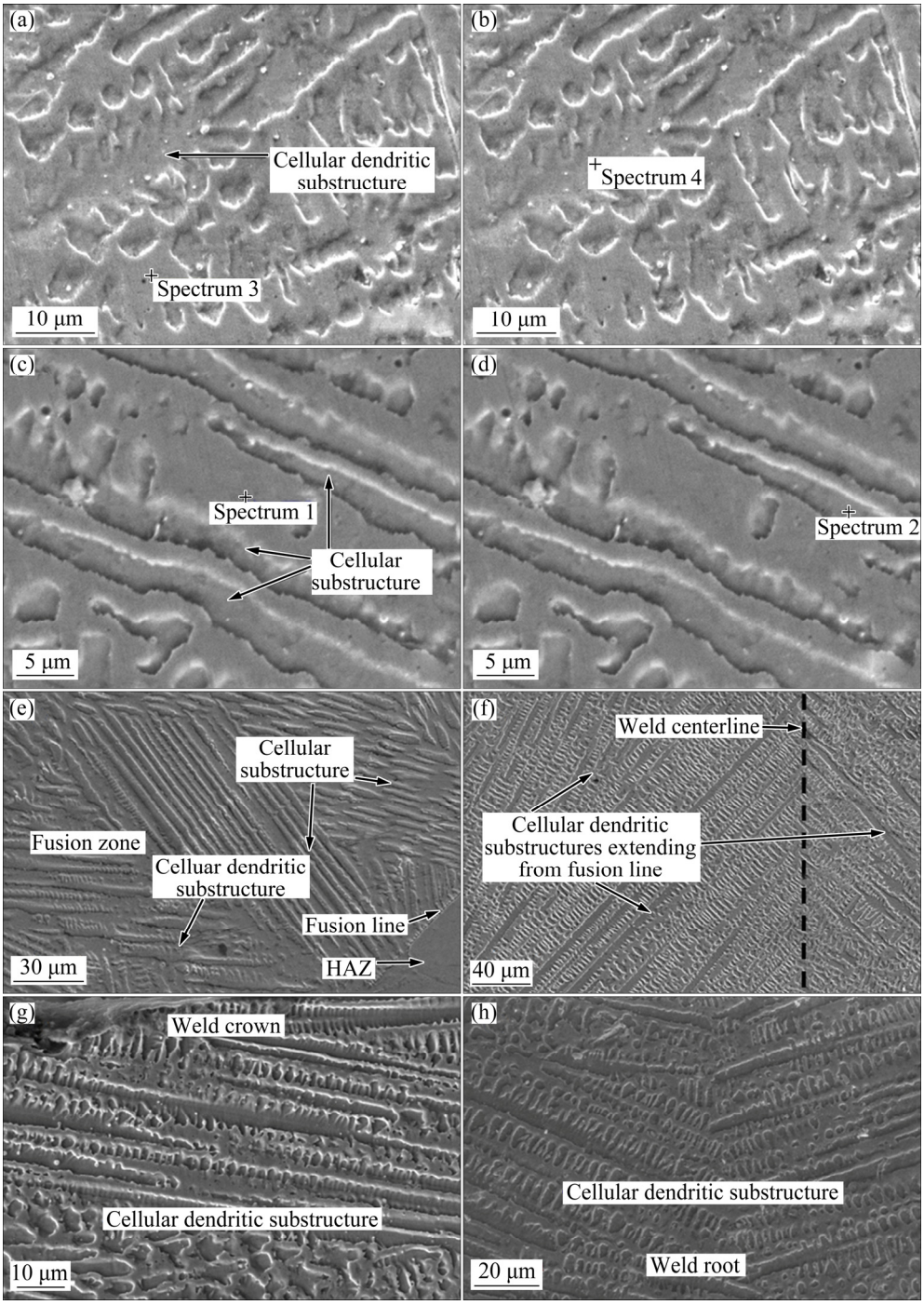

Fig. 3 EDS analysis at interdendritic space (a), dendrite body (b), intercellular space (c), cellular body (d) and SEM images of cellular dendrites formed at fusion line (e), cellular dendritic substructures extending from fusion line to weld centerline (f), cellular dendritic substructures formed at weld crown (g) and weld root (h)

The condition for segregation [42] includes: (1) when segregation ratio is close to 1, elements have low tendency to segregate; (2) when segregation ratio is greater than 1, elements have tendency to segregate towards interdendritic space or intercellular space; and (3) when segregation ratio is less than 1, elements have tendency to segregate towards dendrite body or cellular body. According to the segregation ratio data presented in Table 7, it could be observed that for present investigation: (1) Cr has low tendency to segregate; (2) Mo and W have segregated to interdendritic space or intercellular space; and (3) Ni and Fe have segregated to dendrite body or cellular body. The comparison of segregation ratio of elements showed that the segregation tendency of Ni, Cr, Mo and Fe was found to be less for the present investigation as compared to that reported by

Table 6 EDS analysis of elements within fusion zone at interdendritic space and dendrite body (No. 1−7) as well as intercellular space and cellular body (No. 8−10) for sample welded at laser power of 1000 W and welding speed of 1000 mm/min along with composition of as-received base metal (mass fraction, %)

No.	Site	Ni	Cr	Mo	W	Fe
1	Interdendritic space	54.74	16.82	17.53	4.07	6.84
	Dendrite body	57.22	15.90	16.61	2.99	7.28
2	Interdendritic space	51.55	16.50	20.88	4.88	6.20
	Dendrite body	55.14	16.89	16.79	4.09	7.08
3	Interdendritic space	53.30	16.93	19.52	3.93	6.33
	Dendrite body	56.15	16.70	16.54	3.79	6.82
4	Interdendritic space	53.04	16.66	19.45	4.39	6.46
	Dendrite body	57.20	15.88	16.05	3.99	6.88
5	Interdendritic space	54.27	16.75	18.28	4.98	5.72
	Dendrite body	57.01	16.46	16.02	4.37	6.14
6	Interdendritic space	51.06	16.94	20.47	5.44	6.09
	Dendrite body	55.48	16.76	16.91	4.16	6.69
7	Interdendritic space	56.21	16.29	18.18	3.63	5.69
	Dendrite body	58.43	15.91	16.28	3.20	6.18
8	Intercellular space	53.31	17.10	18.49	4.53	6.57
	Cellular body	56.02	16.64	16.66	3.70	6.98
9	Intercellular space	52.35	16.85	20.40	4.06	6.34
	Cellular body	55.79	16.17	17.69	3.39	6.96
10	Intercellular space	53.51	15.63	19.48	5.34	6.04
	Cellular body	57.73	15.70	16.07	4.24	6.26
11	As-received base metal	55.03	16.18	17.80	4.86	6.13

MA et al [23], which might be due to the high cooling rate.

According to Rosenthal's three-dimensional heat flow equation [40], cooling rate at a point (or in a region of interest) increases with the decrease in linear heat input. An optimized combination of process parameters that include lowest possible value of laser power and highest possible value of welding speed just enough to cause through penetration in Hastelloy C-276 sheet, has been considered as the lowest value of linear heat input in the present investigation. MOSTAAN et al [43] have reported that the combination of higher pulse duration and lower welding speed can result in the reduction in tensile strength of weldment due to the formation of solidification micro-cracks. So, the optimized combination of process parameters might be efficient in reducing the net power consumption as well as increasing the weld productivity without producing any weld defects. The optimized combination for the present investigation has been narrowed down from number of trial runs carried out over a range of welding parameters. Figure 5(a) shows the keyhole-shape weld bead cross-sectional geometry for Hastelloy C-276 sheet welded at optimized combination of laser power of 1 kW and welding speed of 1 m/min. Figure 6 shows the inclination of solidified melt front (or fringe) to the welding direction, where the fringes are superimposed by lines. Figure 6 shows that the optimized value of welding speed chosen in the present investigation has resulted in V-shape of trailing weld pool, which is a characteristic of high speed welding. In addition, Figure 5(a) shows that the width of the heat affected zone is negligible as compared to the width of the weld zone which might be possibly due to lower heat input. FAUZI et al [44] have reported that the width of heat affected zone depends on linear heat input per unit length supplied at the weld joint. Corresponding to Fig. 5(a), Fig. 5(b) shows the FEM image of the weld bead formed under the same welding condition. Hence, an approximate agreement of weld bead geometrical features between experimental and FEM analysis is observed and reported in Table 8. The cooling rate measurement by experiment (as shown in Fig. 5(c)) as well as by FEM (as shown in Fig. 5(d)) at the weld centerline was found to be in the order of 10^3 °C/s.

High cooling rate reduces the solidification time of the mushy zone, and as a result, the time available for diffusion of elements between solid and liquid phase is reduced. This could be observed for Cr, Fe and W from Table 6, where the difference in composition of the above mentioned elements between dendrite body and interdendritic space is less. However, Ni and Mo segregation within the weld zone was observed, but the degree of micro-segregation was less than that in the previous reported literature [23]. Mo and W segregation to interdendritic space could be attributed to solute rejection and consequent enrichment of liquid phase ahead of the solid/liquid interface. Ni and Fe enrichment of the dendrite body might be possibly due to back-diffusion phenomena [40] that occur when solidified zone (i.e. cell/dendrite body) accommodates more Ni solute from the liquid and becomes enriched. Back-diffusion of Ni and Fe in the austenite could occur by means of substitution and/or vacancy formation, and the energy for such diffusion might be available from the evolution of latent heat of fusion during solidification of the melt pool. However, back-diffusion potential (or diffusivity of solute in the solid or dendrite body) for Mo, W was not significant, which might be due to their lower solid-state diffusivity in Ni. DUPONT et al [2] have reported the relation between back-diffusion potential vs cooling rate for alloying elements in Ni base alloy. The plot showed that at any given cooling rate, Fe has higher

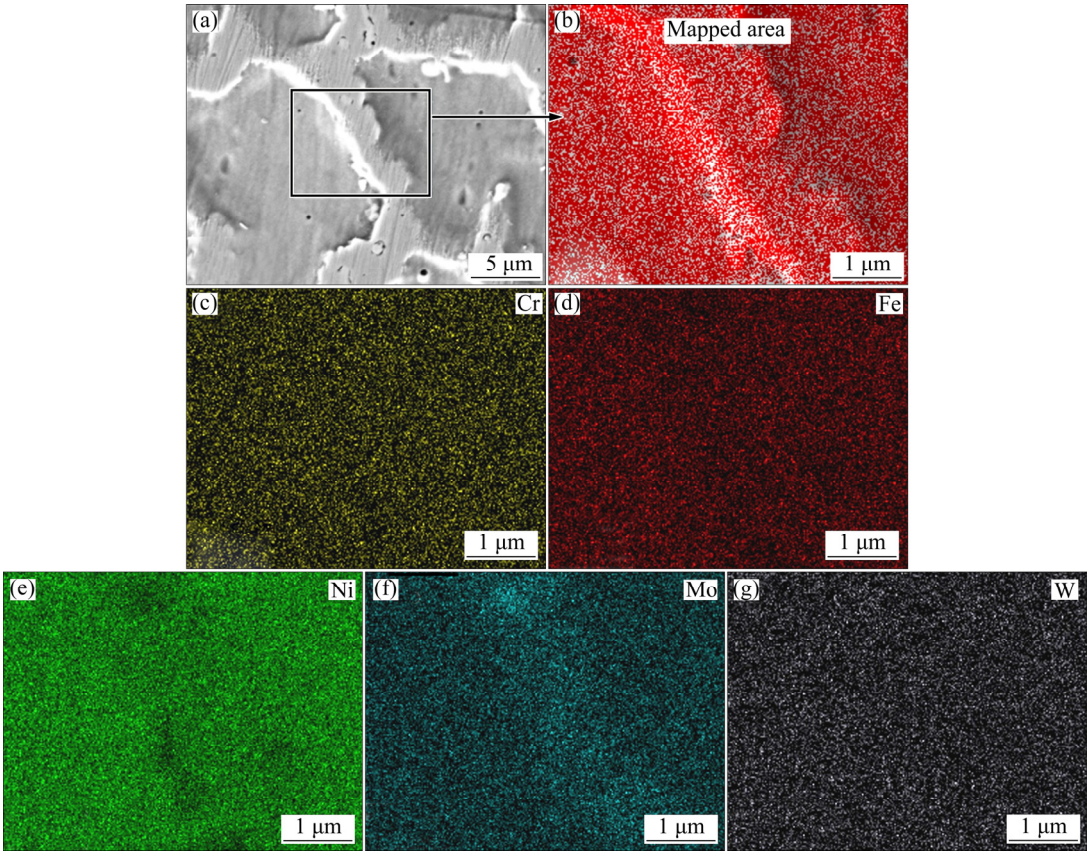

Fig. 4 X-ray maps of volume element for micro-segregation analysis of cellular dendritic substructure (a), enlarged view of mapped area (b) showing distribution of Cr (c), Fe (d), Ni (e), Mo (f) and W (g)

Table 7 Comparison of segregation ratios obtained by different resources

Source		Ni	Cr	Mo	W	Fe
MA et al [23]		0.89*	1.09*	1.28*	1.16*	0.91*
Present investigation	Site 1	0.95	1.05	1.05	1.36	0.93
	Site 2	0.93	0.97	1.24	1.19	0.87
	Site 3	0.94	1.01	1.18	1.03	0.92
	Site 4	0.92	1.04	1.21	1.10	0.93
	Site 5	0.95	1.01	1.14	1.13	0.93
	Site 6	0.92	1.01	1.21	1.30	0.91
	Site 7	0.96	1.02	1.11	1.13	0.92
	Site 8	0.95	1.02	1.10	1.22	0.94
	Site 9	0.93	1.04	1.15	1.19	0.91
	Site 10	0.92	0.99	1.21	1.25	0.96

*Calculated based on data provided in literature [23]

tendency to back-diffuse than Mo and W. Hence, it might be possible that Fe has higher tendency to segregate to solid/dendrite body than the other elements.

The possible reasons for difference in Mo concentration between interdendritic space and dendrite body within fusion zone include: (1) Mo segregation due to formation of finer cellular and cellular dendritic substructures (as shown in Fig. 3) within the weld zone reported by GLICKSMAN [45], (2) low solubility of Mo in matrix due to difference in the atomic radii and crystal structure with Ni (i.e. according to Hume−Rothery rule for substitutional solid solution), and (3) lower tendency for back diffusion [2] due to cooling rate in the order of 10^3 °C/s associated with laser beam welding, as shown in Figs. 5(c) and (d). It is expected that the degree of micro-segregation within the weld zone for the present investigation might not lead to the formation of any secondary intermetallic phases. This could be explained by the time−temperature transformation curve of Hastelloy C-276 as reported by DAVIS [46], in which the aging time has to exceed 360 s to cause precipitation of secondary intermetallic phases. However, according to the thermal cycle plot as shown in Fig. 5(d), cooling time from 1100 to 650 °C is less than 1 s, hence, the possibility of precipitation of secondary intermetallic phases could be the least. LONG et al [47], while carrying out laser cladding of Inconel 718, have observed that high cooling rate lowers the segregation of Nb and reduces the formation of detrimental Laves phase. Figure 7 shows the TEM image of grain in laser welded sample. It could be seen that the grain in as-laser-welded sample shows no observable precipitation of secondary phases. This observation is coherent with AHMAD et al [4], who reported that the formation of the

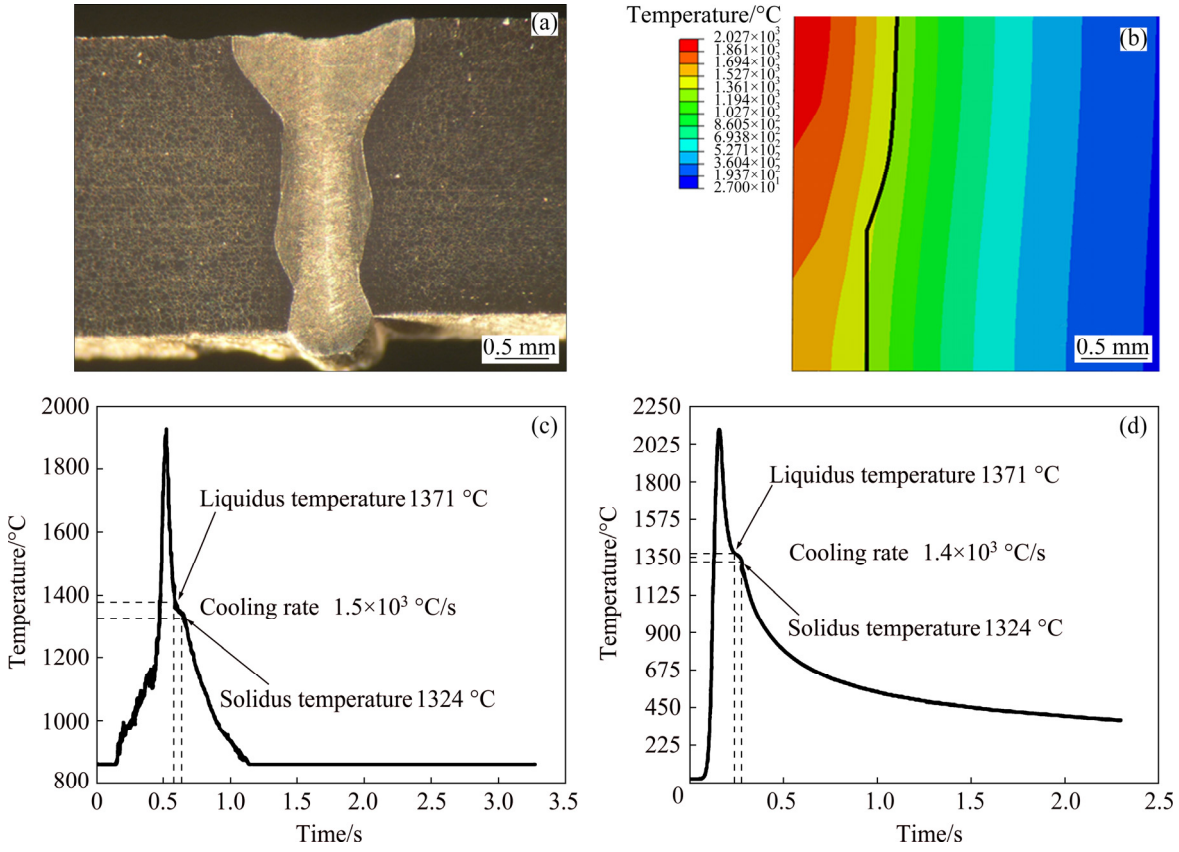

Fig. 5 Optical image of weld bead cross-sectional geometry (a), FEM image of weld bead cross-sectional geometry with temperature scale (b), experimentally measured cooling rate (c) and FEM predicted cooling rate (d) for Hastelloy C-276 sheet welded at laser power of 1 kW and welding speed of 1 m/min

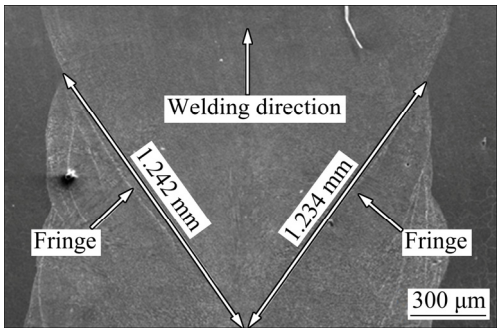

Fig. 6 SEM image of top face of weld zone showing inclination of fringe lines in welding direction

Table 8 Comparison of results obtained by experiment and FEM analysis

Analysis type	Depth of penetration/ mm	Crown width/ mm	Root width/ mm	Peak temperature/ °C	Cooling rate/ (°C·s^{-1})
Experiment	2.70	1.60	0.78	1930	1.5×10^3
FEM	2.70	1.50	0.72	2130	1.4×10^3

secondary intermetallic phase μ was possible only when the electron beam welded Hastelloy C-276 sheet was tempered at 950 °C for 3 h.

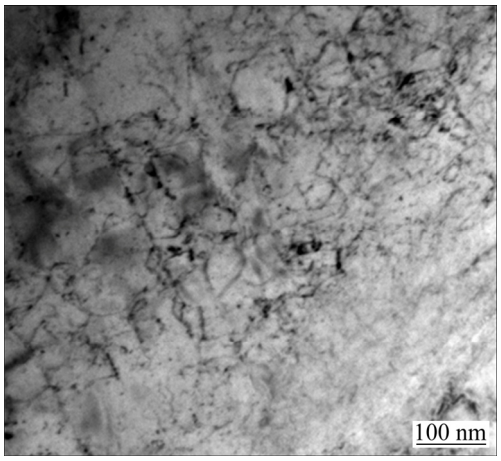

Fig. 7 TEM image of grain in as-laser-welded sample

3.4 Analysis of equilibrium distribution coefficient (k) for elements

Elements with equilibrium distribution coefficient value of 1.00 or greater have lower tendency to segregate to the liquid phase during solidification of the mushy zone. Table 9 shows that Ni, Cr, and Fe have k values higher than 1, while Mo and W have lower values of k. The result is coherent with EDS analysis as shown in Table 6 as well as with the segregation ratio as shown in

Table 7, which shows that Ni, Cr, and Fe have lower tendency to segregate to the interdendritic space or intercellular space. This can be correlated with the observation reported by DUPONT et al [2], that is, the elements with similar atomic radii as those of Ni such as Cr and Fe are likely to have lower segregation tendency. Values of k for Ni, Cr and Mo in the present investigation show a less segregation tendency when compared with the previous literature [23] as represented in Table 7. While the k value for W shows significant tendency for segregation into liquid phase; however, the difference in elemental composition between dendrite body and interdendritic space was found to be insignificant as shown in Table 9. It might be possible that the segregation of W was significant along the length of cellular dendrite rather than between dendrite body and interdendritic space. As compared with the k value of W for the present investigation, k value of W in the previous literature [23] shows lower tendency to segregate towards liquid or interdendritic space. Since segregation ratio (as shown in Table 7) as well as k value (as shown in Table 9) for Cr is equal to 1, and segregation of Mo and W is evident, metal carbides comprising of Mo and W might have formed in the interdendritic space owing to high diffusivity of C in Ni at temperature around 650 °C.

Table 9 Equilibrium distribution coefficients ($k=C_3$ (or C_4)/C_0) for elements [2]

Site No.	Ni	Cr	Mo	W	Fe
1	1.03	0.98	0.93	0.61	1.18
2	1.00	1.04	0.94	0.84	1.15
3	1.02	1.03	0.92	0.77	1.11
4	1.03	0.98	0.90	0.82	1.12
5	1.03	1.01	0.90	0.89	1.00
6	1.00	1.03	0.95	0.85	1.09
7	1.06	0.98	0.91	0.65	1.00
8	1.01	1.02	0.93	0.76	1.13
9	1.01	0.99	0.99	0.69	1.13
10	1.04	0.97	0.90	0.87	1.02

C_0 is composition of element in base metal

4 Conclusions

1) In the present investigation, Keyhole-shape weld bead was obtained for ytterbium fiber laser welded Hastelloy C-276 sheet. In addition, melting efficiency (64%) for fiber laser was found to high as compared with that (48%) reported for conventional moving heat source.

2) The linear heat input per unit thickness of sheet used for the present investigation was substantially reduced than that of previous reported literatures. This is due to high beam quality as well as high power density associated with ytterbium fiber lasers.

3) Micro-segregation of Ni, Cr and Mo within the weld zone was found to be less as compared with the previous reported literature. Hence, the localized concentration gradient of elements within the weld is possible to reduce by suitable use of process parameters.

4) The magnitude of cooling rate in the order of 10^3 °C/s attained in the present investigation could be one of the factors in reducing the degree of micro-segregation.

5) Equilibrium distribution coefficient of the Ni, Cr and Mo in the present investigation showed less segregation tendency than that of previous reported literature.

6) The formation of cellular dendritic substructure in the weld zone is another reason that could result in the reduction of the segregation tendency for the elements in consideration.

Acknowledgements

We are very grateful to all the faculty members, technical staffs and research scholars of Department of Mechanical Engineering, Department of Metallurgical & Materials Engineering, and Central Research Facility, I. I. T. Kharagpur for extending their support in carrying out various experiments.

References

[1] Hastelloy® C-276 alloy H-2002E [R]. Indiana: Haynes International, 2017.

[2] DUPONT J N, LIPPOLD J C, KISER S D. Welding metallurgy and weldability of nickel-base alloys [M]. New Jersey: John Wiley & Sons, 2009.

[3] JUN C H, WANG J Z, YAN F Y, ZHANG Q, LI Q A. Corrosion wear synergistic behavior of Hastelloy C276 alloy in artificial seawater [J]. Transactions of Nonferrous Metals Society of China, 2015, 25: 661−668.

[4] AHMAD M, AKHTER J I, AKHTAR M, IQBAL M, AHMED E, CHOUDHRY M A. Microstructure and hardness studies of the electron beam welded zone of Hastelloy C-276 [J]. Journal of Alloys and Compounds, 2005, 390: 88−93.

[5] WU D J, MA G Y, NIU F Y, GUO D M. Pulsed laser welding of Hastelloy C-276: High temperature mechanical properties and microstructure [J]. Materials and Manufacturing Processes, 2013, 28: 524−528.

[6] SHOEMAKER L E, CRUM J R. Nickel−chromium−molybdenum superalloys: The solution to corrosion problems in wet limestone FGD air pollution control systems [R]. Huntington: Special Metals Corporation, 2009.

[7] Technical knowledge: Difference between heat input and arc energy [R]. Cambridge: The Welding Institute, 2017.

[8] CIESLAK M J, HEADLEY T J, ROMIG A D. The welding metallurgy of Hastelloy alloys C-4, C-22, and C-276 [J]. Metallurgical and Materials Transactions A, 1986, 11: 2035−2047.

[9] ÇAM G, KOÇAK M. Progress in joining of advanced materials [J]. International Materials Reviews, 1998, 43: 1−44.

[10] LI J, SHRESTHA S L, LONG Y, ZHIJUN L, XINTAI Z. The

formation of eutectic phases and hot cracks in one Ni−Mo−Cr superalloy [J]. Materials & Design, 2016, 93: 324−333.

[11] SIHOTANG R, SUNGSANG P, EUNGRYUL B. Effects of heat input on microstructure of tungsten inert gas welding used Hastelloy X [J]. Materials Research Innovations, 2014, 18: 1074−1080.

[12] ÇAM G, DOS SANTOS J F, KOCAK M, FISCHER A, RATJEN R. Properties of laser beam welded superalloys Inconel 625 and 718 [C]// Proc 7th European Conference on Laser Treatment of Materials 1998. Hannover: Werkstoff-Informationsgeselschaft mbH, 1998: 333−338.

[13] ÇAM G, KOÇAK M. Progress in joining of advanced materials. Part 1: Solid state joining, fusion joining, and joining of intermetallics [J]. Science and Technology of Welding and Joining, 1998, 3:105−126.

[14] ÇAM G, İPEKOĞLU G. Recent developments in joining of aluminum alloys [J]. International Journal of Advanced Manufacturing Technology, 2017, 91: 1851−1866.

[15] THIRUNAVUKARASU G, CHATTERJEE S, KUNDU S. Scope for improved properties of dissimilar joints of ferrous and non-ferrous metals [J]. Transactions of Nonferrous Metals Society of China, 2017, 27: 1517−1529.

[16] ADABI M, AMADEH A A. Formation mechanisms of Ni−Al intermetallics during heat treatment of Ni coating on 6061 Al substrate [J]. Transactions of Nonferrous Metals Society of China, 2015, 25: 3959−3966.

[17] XU W C, HUANG K, WU S F, ZONG Y Y, SHAN D B. Influence of Mo content on microstructure and mechanical properties of β-containing TiAl alloy [J]. Transactions of Nonferrous Metals Society of China, 2017, 27: 820−828.

[18] QUAN L I, WU A P, LI Y J, WANG G Q, QI B J, YAN D Y, XIONG L Y. Segregation in fusion weld of 2219 aluminum alloy and its influence on mechanical properties of weld [J]. Transactions of Nonferrous Metals Society of China, 2017, 27: 258−271.

[19] ZOU X L, HONG Y A, CHEN X H. Evolution of second phases and mechanical properties of 7075 Al alloy processed by solution heat treatment [J]. Transactions of Nonferrous Metals Society of China, 2017, 27: 2146−2155.

[20] MORITA K, YOSHIKAWA T. Thermodynamic evaluation of new metallurgical refining processes for SOG−silicon production [J]. Transactions of Nonferrous Metals Society of China, 2011, 21: 685−690.

[21] QIN H U, LIN L I, ZHAO X B, GAO S F, ZHANG J, FU H Z. Effect of carbon and boron additions on segregation behavior of directionally solidified nickel-base superalloys with rhenium [J]. Transactions of Nonferrous Metals Society of China, 2013, 23: 3257−3264.

[22] LUO Y, ZHANG Q, JIANG W, ZHANG Y, HAO M, TU S T. The microstructure, mechanical properties and fracture behavior of hastelloy C276−BNi_2 brazed joint [J]. Materials & Design, 2017, 115: 458−466.

[23] MA G Y, WU D J, GUO D M. Segregation characteristics of pulsed laser butt welding of Hastelloy C-276 [J]. Metallurgical and Materials Transactions A, 2011, 42: 3853−3857.

[24] WU D J, MA G Y, GUO Y Q, GUO D M. Study of weld morphology on thin Hastelloy C-276 sheet of pulsed laser welding [J]. Physics Procedia, 2010, 5: 99−105.

[25] MANIKANDAN M, ARIVAZHAGAN N, RAO M N, REDDY G M. Improvement of microstructure and mechanical behaviour of gas tungsten arc weldments of Alloy C-276 by current pulsing [J]. Acta Metallurgica Sinica, 2015, 28: 208−215.

[26] QUINTINO L, COSTA A, MIRANDA R, YAPP D, KUMAR V, KONG C J. Welding with high power fiber lasers—A preliminary study [J]. Materials & Design, 2007, 28: 1231−1237.

[27] COSTA A, MIRANDA R, QUINTINO L, YAPP D. Analysis of beam material interaction in welding of titanium with fiber lasers [J]. Materials and Manufacturing Processes, 2007, 22: 798−803.

[28] LU J, CHOI E S, ZHOU H D. Physical properties of Hastelloy® C-276™ at cryogenic temperatures [J]. Journal of Applied Physics, 2008, 103: 064908.

[29] HASHIM M, BABU K S, DURAISELVAM M, NATU H. Improvement of wear resistance of Hastelloy C-276 through laser surface melting [J]. Materials & Design, 2013, 46: 546−551.

[30] MOHAMED A, MOHAMED T. Ni-based Cr alloys and grain boundaries characterization [J]. International Journal of Computational Engineering Research, 2013, 3: 69−72.

[31] MUVVALA G, KARMAKAR D P, NATH A K. Monitoring and assessment of tungsten carbide wettability in laser cladded metal matrix composite coating using an IR pyrometer [J]. Journal of Alloys and Compounds, 2017, 714: 514−521.

[32] DAL M, FABBRO R. An overview of the state of art in laser welding simulation [J]. Optics & Laser Technology, 2016, 78: 2−14.

[33] PIEKARSKA W, KUBIAK M. Theoretical investigations into heat transfer in laser-welded steel sheets [J]. Journal of Thermal Analysis and Calorimetry, 2012, 110: 159−166.

[34] LIU C C, HE J S. Numerical analysis of thermal fluid transport behavior during electron beam welding of 2219 aluminum alloy plate [J]. Transactions of Nonferrous Metals Society of China, 2017, 27: 1319−1326.

[35] ZHANG B G, TING W A, DUAN X H, CHEN G Q, FENG J C. Temperature and stress fields in electron beam welded Ti-15-3 alloy to 304 stainless steel joint with copper interlayer sheet [J]. Transactions of Nonferrous Metals Society of China, 2012, 22: 398−403.

[36] GUO Y Q, WU D J, MA G Y, GUO D M. Trailing heat sink effects on residual stress and distortion of pulsed laser welded Hastelloy C-276 thin sheets [J]. Journal of Materials Processing Technology, 2014, 214: 2891−2899.

[37] DAVIS J R. ASM specialty handbook: Nickel, cobalt, and their alloys [M]. Ohio: ASM International, 2000.

[38] WALSH C A. Laser welding−Literature review [R]. Cambridge: University of Cambridge, 2002.

[39] STENBACKA N, CHOQUET I, HURTIG K. Review of arc efficiency values for gas tungsten arc welding [R]. Trollhättan: University West, 2018.

[40] KOU S. Welding metallurgy [M]. 2nd ed. New Jersey: John Wiley & Sons, 2003.

[41] LAMPMAN S. Weld integrity and performance [M]. Ohio: ASM International, 1997.

[42] ZHANG Y, LI J. Characterization of the microstructure evolution and microsegregation in a Ni-based superalloy under super-high thermal gradient directional solidification [J]. Materials Transactions, 2012, 53: 1910−1914.

[43] MOSTAAN H, SHAMANIAN M, HASANI S, SAFARI M, SZPUNAR J A. Nd: YAG laser micro-welding of ultra-thin FeCo−V magnetic alloy: Optimization of weld strength [J]. Transactions of Nonferrous Metals Society of China, 2017, 27: 1735−1746.

[44] FAUZI E I, JAMIL M C, SAMAD Z, MUANGJUNBUREE P. Microstructure analysis and mechanical characteristics of tungsten inert gas and metal inert gas welded AA6082-T6 tubular joint: A comparative study [J]. Transactions of Nonferrous Metals Society of China, 2017, 27: 17−24.

[45] GLICKSMAN M E. Principles of solidification: An introduction to modern casting and crystal growth concepts [M]. New York: Springer, 2011.

[46] DAVIS J R. Corrosion of weldments [M]. Ohio: ASM International, 2006.

[47] LONG Y T, NIE P L, LI Z G, HUANG J, XIANG L I, XU X M. Segregation of niobium in laser cladding Inconel 718 superalloy [J]. Transactions of Nonferrous Metals Society of China, 2016, 26: 431−436.

激光焊接哈氏合金 C-276 薄板的元素微偏析特性

Kalinga Simant BAL[1], Jyotsna DUTTA MAJUMDAR[2], Asimava ROY CHOUDHURY[1]

1. Department of Mechanical Engineering, Indian Institute of Technology, Kharagpur, West Bengal 721302, India;
2. Department of Metallurgical & Materials Engineering,
Indian Institute of Technology, Kharagpur, West Bengal 721302, India

摘　要：研究镱纤维激光焊接哈氏合金 C-276 薄板焊缝区的元素微偏析特性。通过 EDS 数据分析得到的偏析比和元素的平衡分布系数表明，与以往报道的激光焊接哈氏合金 C-276 相比，镱纤维激光焊接哈氏合金元素微偏析减少。镱光纤激光器的高熔融效率、低线性输入热量及糊状区较高的冷却速率导致微偏析减少。用镱光纤激光器焊接哈氏合金 C-276 的熔融效率为 64%，比传统焊接方法的熔融效率(48%)高。高熔融效率导致焊接所需的线性热输入减少，因此在本研究中发现，与以往的报道相比，其减幅更大。焊缝中心线从液相温度到固相温度的冷却速率量级为 10^3 °C/s。在焊缝中心线形成了构成较低微偏析的胞状枝晶子结构。

关键词：哈氏合金 C-276；激光焊接；纤维激光器；微偏析

(Edited by Wei-ping CHEN)